Stacked Magma Lenses Beneath Mid-Ocean Ridges: Insights From New Seismic Observations and Synthesis With Prior Geophysical and Geologic Findings

Suzanne M. Carbotte[1] , Milena Marjanović[2] , Adrien F. Arnulf[3] ,
Mladen R. Nedimović[4] , Juan Pablo Canales[5] , and Gillean M. Arnoux[6]

[1]Department of Marine Geology and Geophysics, Lamont-Doherty Earth Observatory, Columbia University, Palisades, NY, USA, [2]Université de Paris, Institut de Physique du Globe de Paris, CNRS, Paris, France, [3]Jackson School, Institute for Geophysics, University of Texas at Austin, Austin, TX, USA, [4]Department of Earth and Environmental Sciences, Dalhousie University, Halifax, NS, Canada, [5]Department of Geology and Geophysics, Woods Hole Oceanographic Institution, Woods Hole, MA, USA, [6]Department of Earth Sciences, University of Oregon, Eugene, OR, USA

Abstract Recent multi-channel seismic studies of fast spreading and hot-spot influenced mid-ocean ridges reveal magma bodies located beneath the mid-crustal Axial Magma Lens (AML), embedded within the underlying crustal mush zone. We here present new seismic images from the Juan de Fuca Ridge that show reflections interpreted to be from vertically stacked magma lenses in a number of locations beneath this intermediate-spreading ridge. The brightest reflections are beneath Northern Symmetric segment, from ∼46°42′-52′N and Split Seamount, where a small magma body at local Moho depths is also detected, inferred to be a source reservoir for the stacked magma lenses in the crust above. The imaged magma bodies are sub-horizontal, extend continuously for along-axis lengths of ∼1–8 km, with the shallowest located at depths of ∼100–1,200 m below the AML, and are similar to sub-AML bodies found at the East Pacific Rise. At both ridges, stacked sill-like lenses are detected beneath only a small fraction of the ridge length examined and are inferred to mark local sites of higher melt flux and active replenishment from depth. The imaged magma lenses are focused in the upper part of the lower crust, which coincides with the most melt rich part of the crystal mush zone detected in other geophysical studies and where sub-vertical fabrics are observed in geologic exposures of oceanic crust. We infer that the multi-level magma accumulations are ephemeral and may result from porous flow and mush compaction, and that they can be tapped and drained during dike intrusion and eruption events.

1. Introduction

Magmatic systems on Earth are composed of bodies of magma [melt-crystal mixtures with high (>30%–50%) melt content], higher crystallinity regions with lower percentages of distributed melt referred to as mush zones (<30%–50% melt), and super-solidus (<1% melt) and sub-solidus host rock (Sparks et al., 2019). Discrete bodies of magma may be volumetrically quite limited in most volcanic systems and may form within mush zones due to different processes of intrusion, mush remobilization, and melt segregation via buoyancy and compaction (Cashman et al., 2017; Sparks et al., 2019). At fast and intermediate spreading mid-ocean ridges (MOR), the architecture of the magmatic system includes a thin (<100 m thick), narrow (∼1–2 km), and laterally extensive (tens of km) axial magma lens (AML) that resides in the mid-crust beneath the sheeted dikes of the upper crust and above a broader crystal mush zone that may extend to the base of the lower crust (e.g., Detrick et al., 1993; Dunn et al., 2000; Kent et al., 1994; Sinton & Detrick, 1992; Vera et al., 1990). The presence of a crystal mush zone is inferred from an ∼5-km wide region of lower seismic velocities and high attenuation attributed to high temperatures with moderate to low fractions (∼2%–30%) of distributed melt (Arnoux et al., 2019; Crawford et al., 1999; Dunn et al., 2000; Vera et al., 1990; Wilcock et al., 1992; Zha et al., 2014). Below the crust, a 10–20 km wide reservoir centered beneath the ridge axis with melt fractions of up to 10% or more is found in the uppermost mantle (Arnoux et al., 2019; Canales et al., 2014; Dunn et al., 2000; Toomey et al., 2007). In a few locations, subhorizontal magma lenses have been detected within this region or embedded within the Moho transition zone (Crawford et al., 1999; Garmany, 1989; Nedimović et al., 2005).

These geophysical observations of a mid-crustal AML located at the base of the sheeted dikes and above a crystal mush zone that spans the lower crust have provided the framework for numerous studies of igneous processes and crustal formation at fast and intermediate spreading ridges over the past 30 years. The evolved compositions of mid-ocean ridge basalts (MORB) relative to mantle derived magmas require shallow level differentiation in magma reservoirs (Grove et al., 1992) and numerous studies consider the AML to play a primary role in the crystallization and evolution of magmas that intrude and erupt at fast spreading ridges to form the upper crust (Karson et al., 2002; Phipps Morgan & Chen, 1993; Rubin & Sinton, 2007; Sinton & Detrick, 1992). Cooling and crystallization of magmas within the AML may also contribute to the formation of the gabbro section that makes up the lower crust with "gabbro glacier" models proposing that the majority of the lower crust forms by downward and outward flow of cumulates formed within the AML (Henstock et al., 1993; Nicolas et al, 1988, 1993; Phipps Morgan & Chen, 1993). However, other observations indicate magma accumulations form and crystallization occurs at multiple levels in the crust (e.g., Coogan, 2014; Maclennan et al., 2004). Studies of the Oman ophiolite, believed to be an analog of fast spread crust, indicate that much of the gabbroic section that makes up the lower crust forms *in situ* through emplacement and crystallization of thin sub-horizontal magma intrusions with melts periodically extracted from these deep sill-like magma bodies to form the upper crustal lavas and dikes (Kelemen et al., 1997; Korenaga & Kelemen, 1998). Geochemical observations on depths of crystallization derived from MORB melt inclusions at a number of MOR sites indicate that while significant melt storage and crystallization occur within the AML, crystallization also occurs deeper in the crust and perhaps shallowest mantle, at all spreading rates (Wanless & Behn, 2017; Wanless & Shaw, 2012).

Until recently, geophysical evidence for discrete magma bodies within the crust at MOR below the AML has been lacking. However, in two separate studies of high-density multi-channel seismic (MCS) data from the axis of the East Pacific Rise (EPR), deeper magma accumulations were detected (Arnulf, Singh, & Pye, 2014; Marjanović et al., 2014, 2018). More recent observations from the Galapagos Spreading Center (GSC, Boddupalli & Canales, 2019) and the Axial seamount hotspot volcano (Carbotte et al., 2020) image similar structures. The magma bodies imaged in these studies are located at depths of ∼1.7–4.5 km below seafloor and are inferred to arise from thin magma sills similar to the AML forming a vertically stacked complex of sub-horizontal magma lenses. These magma accumulations may play an important role in melt ascent, differentiation, and evolution through the crust and may be drained during eruptions (Carbotte et al., 2020; Marjanović et al., 2014).

In this study, analysis of MCS data from the intermediate spreading (56 km/my) Juan de Fuca (JdF) Ridge is presented, revealing vertically stacked sub-horizontal reflections interpreted as magma lenses within the mush zone beneath the AML at each of the surveyed primary spreading segments. Properties of these sub-AML (SAML) bodies are compared to those imaged elsewhere and implications for processes of melt transport in the lower crust and formation of sill-like magma lenses within the extensional MOR setting are considered. We compare characteristics of the stacked magma lenses with observations on the distribution of magma in the crust from other collocated geophysical studies. Finally, observations of these stacked magma lenses are compared with the record of crustal formation in lower crustal exposures on the seafloor and at ophiolite analogs and broader implications for the formation of the lower crust are considered.

2. Data and Analysis Methods

MCS data were collected using the R/V M. Ewing during expedition EW0207 and included along-axis lines spanning the length of the JdF Ridge from Cleft segment in the south to Endeavor segment in the north (Figure 1). Along-axis seismic transects of Vance, Cleft, and Endeavor segments were previously published in separate studies by Canales et al. (2005; 2006) and Van Ark et al. (2007) and along-axis sections from all segments contributed to the interpretations presented in Carbotte et al. (2006). These studies focused on the AML reflection detected beneath the ridge axis in these regions as well as the base of layer 2A event (corresponds with a high porosity gradient in uppermost crust, roughly basalt/dike boundary in young crust). MCS data from Axial Seamount were also acquired during this survey and presented in Arnulf, Harding, et al. (2014, 2018) and Carbotte et al. (2020). In the current study, along-axis lines for the primary spreading segments of the JdF Ridge are reprocessed and the previously unpublished lines from CoAxial and Northern Symmetric segments are presented.
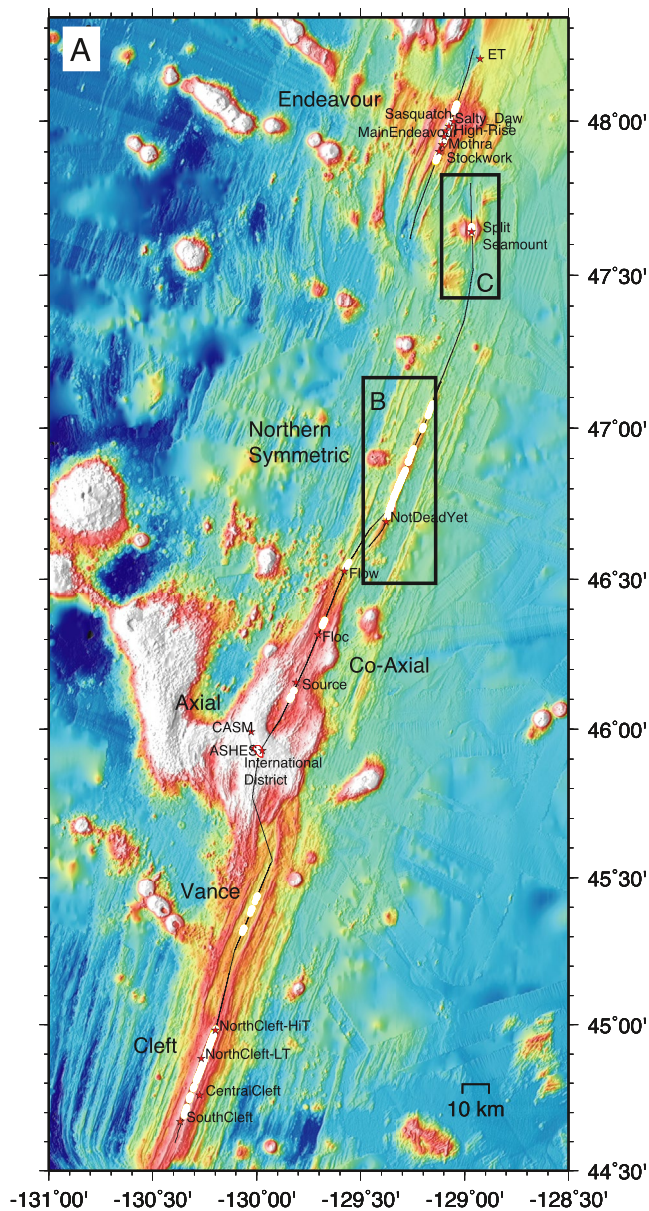
Figure 1. Bathymetric map of the study region with the locations of detected magma lenses beneath the AML indicated. (a) Black lines show trackline locations for data used in this study; extent of sub-AML events are shown in white; locations (red stars) and names of hydrothermal vents and vent fields along the axis are indicated (from InterRidge Vent Database [Beaulieu & Szafrański, 2020]). Rectangles show locations of close up maps shown in (b) and (c). At Axial Seamount, the location of the column of magma sills beneath the Main Magma Reservoir from Carbotte et al. (2020) is shown in red outline. (b) Close up bathymetry of the southern portion of Northern Symmetric segment. Black rectangle shows location of seismic section in Figure 2a; location of CMPs along track are indicated with small black dots every 100 CMPs, large dots and labels every 500 CMPs; blue star shows location of superCMP shown in Figure 2b. (c) Close up bathymetry of the Split Seamount portion of Northern Symmetric segment. Black rectangle shows location of seismic section in Figure 3a; blue star indicates location of superCMP in Figure 3b. Other annotation as in parts (a) and (b).

MCS data were acquired with a tuned 10 air gun, 3,005 cu. in. (49.2 L) source array with shots fired every 37.5 m along track and a 6-km-long 480 channel Syntron digital streamer with receiver groups spaced at 12.5 m. Nominal common midpoint (CMP) gather spacing is 6.25 m, providing a data trace fold of 80. The recorded signal has a bandwidth ranging from 2 to over 100 Hz and a dominant frequency of 10–30 Hz. The data are processed using the same prestack and poststack sequence described in Carbotte et al. (2008). Prestack processing includes F-K and bandpass (2–7–100–125 Hz) filtering, amplitude correction for geometrical spreading, predictive deconvolution, and trace editing, followed by CMP sort, velocity analysis, normal move-out corrections to align the signal for stacking, and CMP mute. Poststack processing includes seafloor mute, primary multiple mute to reduce migration noise, bandpass filtering (2–7–20–40 Hz at Moho depth), and time migration to collapse diffractions and correctly position reflections. Processing for the layer 2 A/2B event, a refracted arrival detected at large source-receiver offsets, follows the modified processing sequence described in detail in Nedimović et al. (2008). Optimal normal move-out velocities that best flatten the retrograde branch of the layer 2A refraction are chosen from constant velocity stacks using the mid-offset range of the streamer (1,500–3,500 m). The stacked layer 2A event is time migrated and coherency filtered. Surgical mute is then used to extract the layer 2A event, which is merged with the crustal section to form the final composite seismic images (Figures 2, 3, and S1–S6). From these sections, primary seismic horizons detected beneath the ridge axis including the layer 2A event, AML, SAML, as well as sparse Moho reflections are digitized and converted to depth beneath seafloor using a constant interval velocity of 2.65 km/s for layer 2A, 5.5 km/s for layer 2B, and mid-crust SAML events and 6.5 km/s for the region below. In Figure 4, we show a composite along-axis interpretation that also includes digitized horizons corresponding to the Main Magma Reservoir (MMR) and deeper magma lens conduit beneath Axial Seamount presented in Arnulf, Harding, et al. (2014) and Carbotte et al. (2020), respectively.

3. Results and Interpretation

3.1. AML and SAML Reflections

The new processed sections show the layer 2A event and bright reflections from the AML beneath all segments of the JdF Ridge, which were the focus of the earlier studies using the EW0207 seismic dataset. However, in addition to these events, the new images show a series of reflections beneath the AML in a number of locations (labeled SAML, Figures 1–3 and S1–S6). The brightest SAML events are detected beneath the Northern Symmetric segment within an approximately 18 km length of the ridge from ~46°42'–52'N (Figure 2), and at the northern end of this segment beneath Split Seamount centered at 47°39'N (Figure 3). Other fainter events are detected intermittently beneath Endeavor, CoAxial, Vance, and Cleft segments (Figures 1, 4, S2, S3, and S6). These SAML events correspond with quasi-horizontal reflections that extend continuously for along-axis lengths of ~1–8 km and are located at a range of two-way travel times (twtt) below the AML (50–450 ms, inferred depths of 100–1,200 m assuming velocities of 5.5 km/s). In a number of locations additional deeper but typically fainter events are imaged forming a vertically stacked cluster of events similar to those
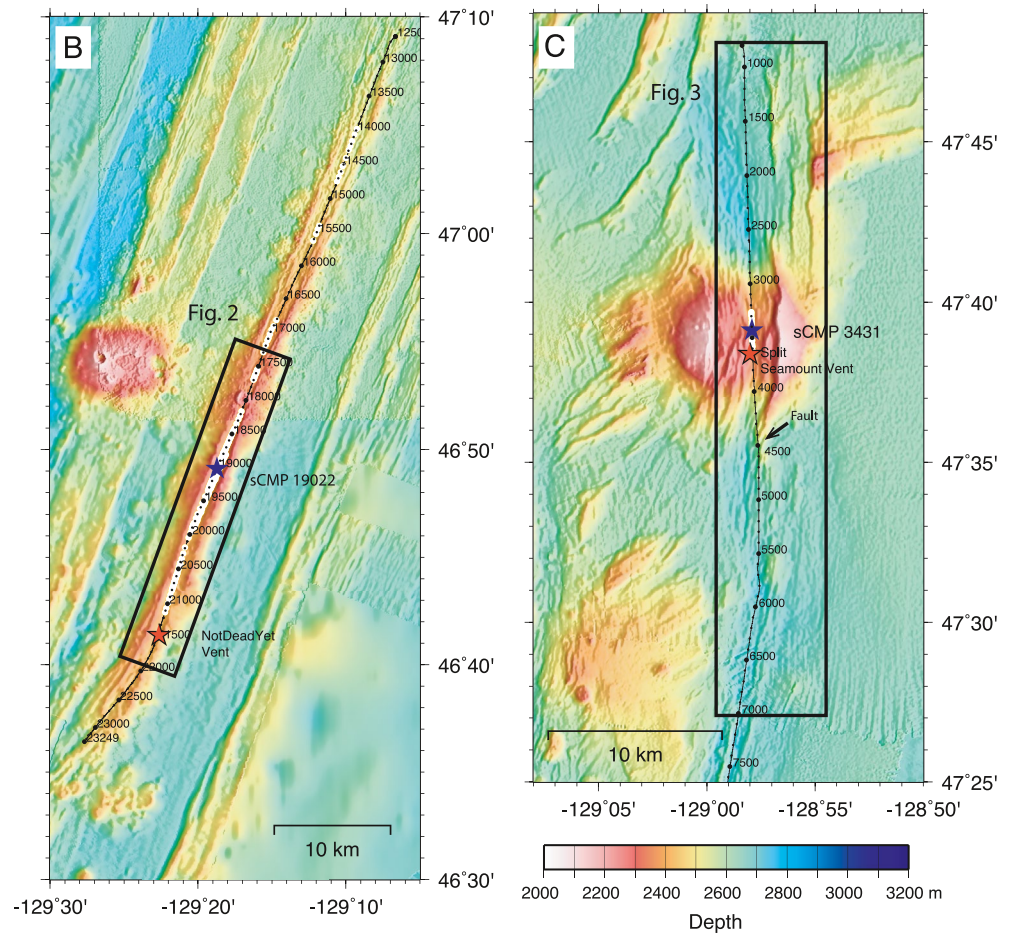
Figure 1. *Continued*

observed beneath Axial Seamount (Figure 4). These clusters of deeper reflections are most prominent beneath Split Seamount where three events are detected below the AML spaced ~150–225 ms apart (Figure 3). Prestack data from a region along Northern Symmetric where seafloor is relatively smooth and hence image quality is higher than elsewhere show the AML, as well as the first SAML event, as bright reflections which can be traced across source-receiver offsets of ~0–3,000 m with the highest amplitude signals at near offsets that are well-flattened at approximately the same moveout velocity as for the AML above (2,700 km/s, Figure 2b). A second lower amplitude event is also evident in the pre-stack CMP gather at a two-way travel time of 4,600 ms, which can also be traced to mid-offsets. A third deeper possible event in the stack section corresponds with faint energy confined to near offsets in the CMP gather (Figures 2a cf. 2b).

The SAML reflections detected in our study indicate that zones of abrupt impedance contrast are present beneath the AML along the JdF Ridge. Given the predicted high temperatures in the crust beneath the AML (>1,100°C), abrupt impedance contrasts in this region are most plausibly due to the presence of embedded magma bodies. Long-streamer MCS data support the application of waveform modeling and other methods which have been used to constrain properties of the AML and the surrounding matrix in several MOR locations including the Cleft segment of the JdF Ridge. From 1-D waveform inversion of the AML reflection at two sites along Cleft segment (44°59′N and 44°40.05′N), Canales et al. (2006) infer that the AML is a thin body <100 m thick, containing high percent of melt (estimates of 60%–75% and 30%, respectively) and floored by a partially solid matrix. Optimal velocity models indicate velocities below the AML of 5.9–6.2 km/s, well above the minimum velocities of 3.7 and 5.0 km/s within the magma lens at the two locations.
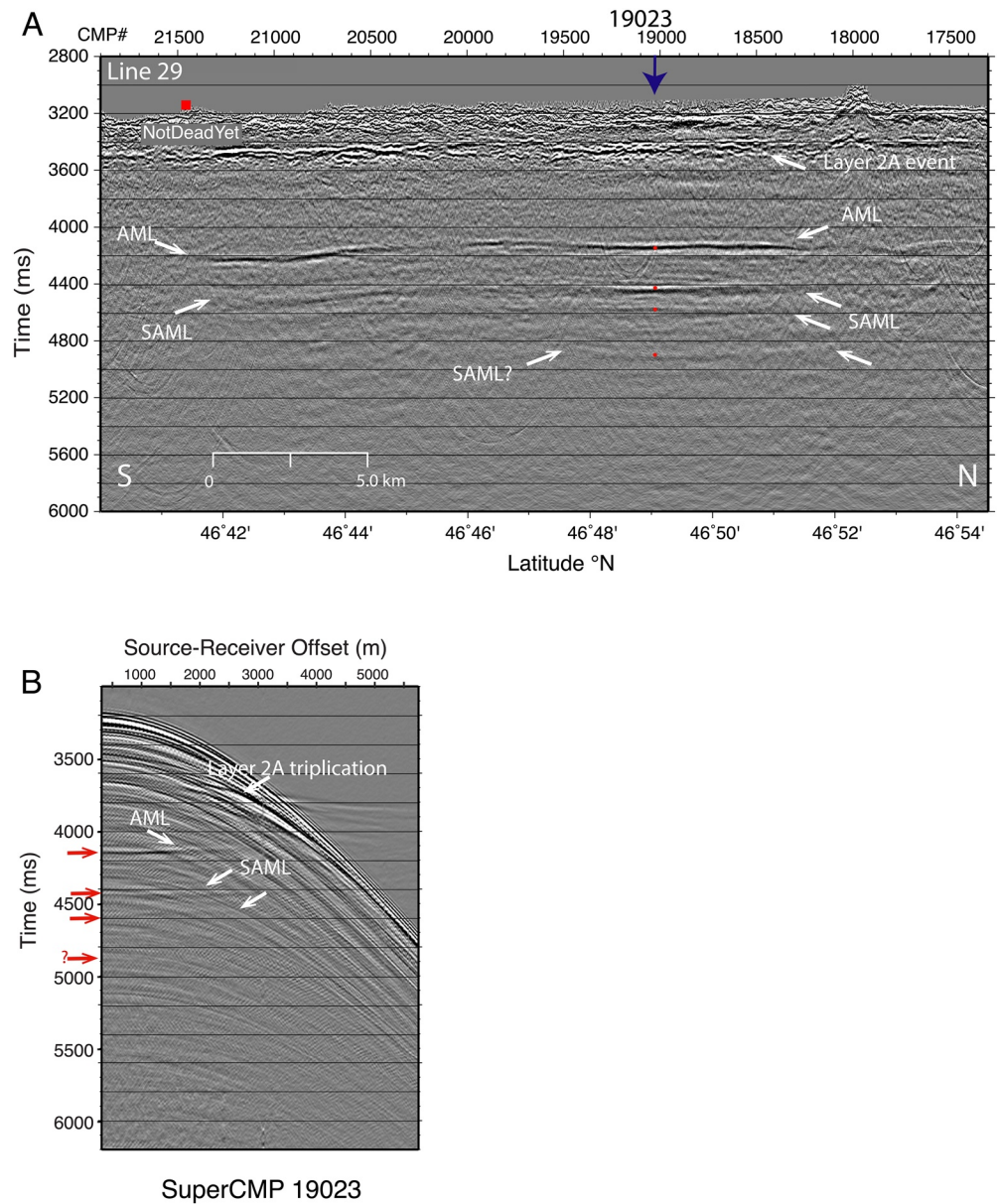
Figure 2. Portion of along-axis seismic Line 29 from southern end of Northern Symmetric segment showing the AML and deeper sub-AML (SAML) reflections. (a) Migrated along-axis seismic section. Location of hydrothermal vent (Not Dead Yet) and superCMP 19023 shown in (b) are indicated. Red dots correspond to AML and SAML events indicated with red arrows on the superCMP shown in panel (b). (b) SuperCMP gather created by stacking 12 adjacent CMPs centered at CMP 19023, with bandpass filter (2-7-40-60 Hz) and a constant moveout velocity of 2700 m/s applied. Two SAML events can be detected, both clearly evident at near offsets like the AML event above, and both can be traced into the far offsets. There is a third possible deeper event in the stacked section but this is a much fainter event in the prestack gather. Red arrows along vertical axis indicate location of these events on stacked section in panel (a).

In the current study, SAML events are identified beneath the more melt rich 44°59′N site analyzed by Canales et al. (2006). Although the signal-to-noise ratio (S/N) of the SAML reflections observed here and elsewhere along the JdF Ridge is too low for similar quantitative analysis, some information on the nature of these events can be derived from other properties of these reflections. First, the hot sub-AML environment should be highly attenuating in the presence of melt. That we are able to image a series of reflections below the AML requires limited seismic attenuation at the frequencies of our imaging source consistent with the partially solid mush matrix inferred to underlie the AML in the waveform modeling study from Cleft
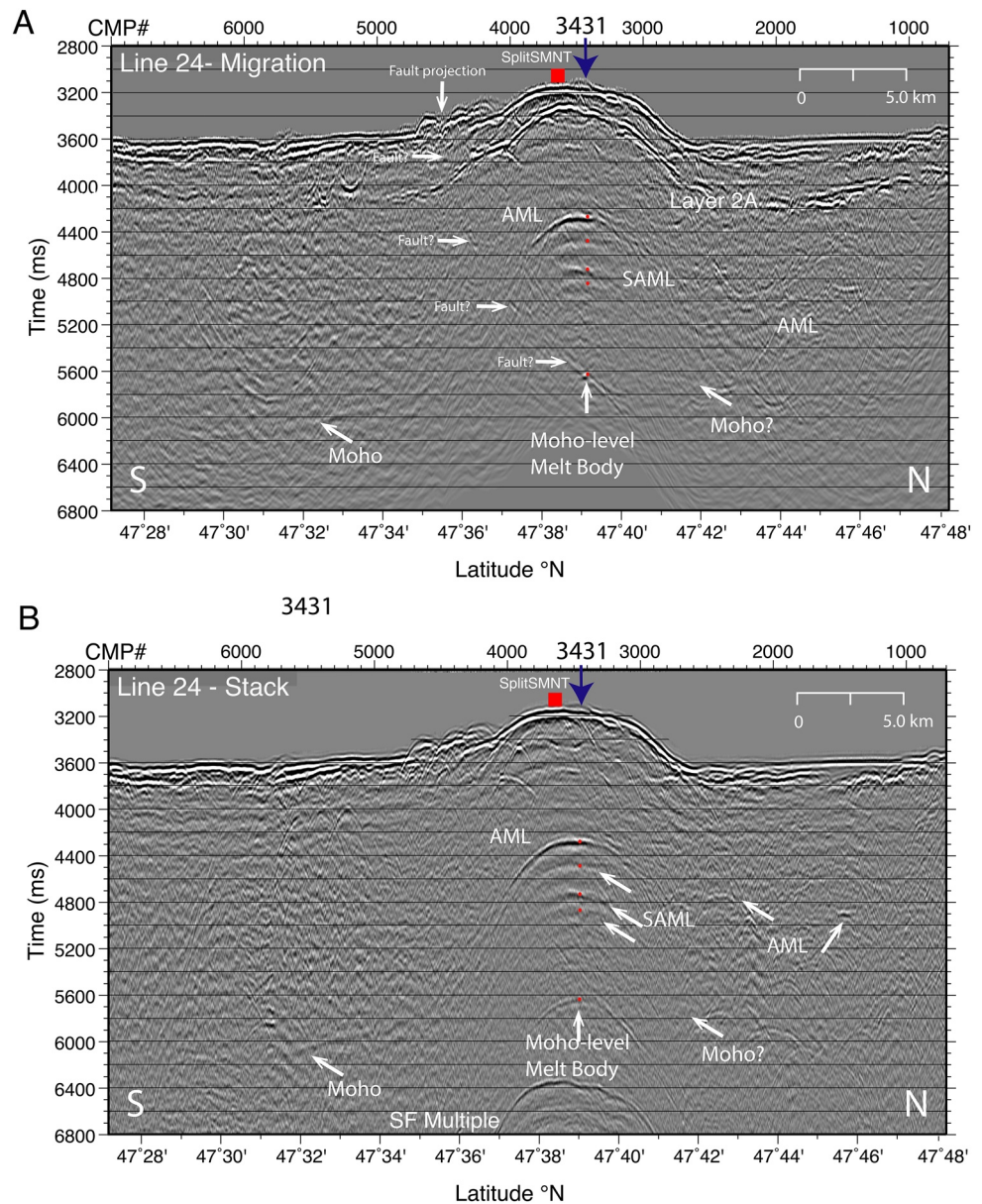
Figure 3. Portion of along-axis seismic Line 24 from northern end of Northern Symmetric segment following the ridge axis where it bisects Split Seamount. (a) Migrated along-axis seismic section. Multiple levels of SAML events are located beneath the AML reflection as well as a small bright reflector interpreted to be a magma body located beneath Moho. Intermittent reflections from possible trans-crustal fault are also identified. Location of the Split Seamount hydrothermal vent (red square) and superCMP 3431 (blue arrow) shown in panels c and d are indicated. Red dots on section correspond to events indicated with red arrows on the superCMP panels. (b) Stack section. The stack section shows the broad diffractions associated with the AML and SAML events and the interpreted Moho level melt body. (c) SuperCMP gather 3431 illustrating the AML, SAML and Moho level reflections. Gather is created by stacking 12 adjacent CMPs, with bandpass filter as well as AGC applied in order to highlight the deeper events. Red arrows along vertical axis indicate traveltime of these events on stacked/migrated sections in [panels (a) and (b)]. (d) Gather with variable moveout velocity applied to flatten the AML, SAML and Moho body events.

segment. For the simplifying assumption of a similar background matrix velocity, some constraints on the maximum thickness of the AML and SAML reflecting bodies can be derived from the dominant frequency of the reflections. Assuming a matrix P-wave velocity of 5.5 km/s below the AML, dominant frequencies of the AML (11–12 Hz) and SAML (8–10 Hz) events along Northern Symmetric gives maximum thicknesses of 115–125 m and 138–170 m, respectively if the reflections arise from a single body.
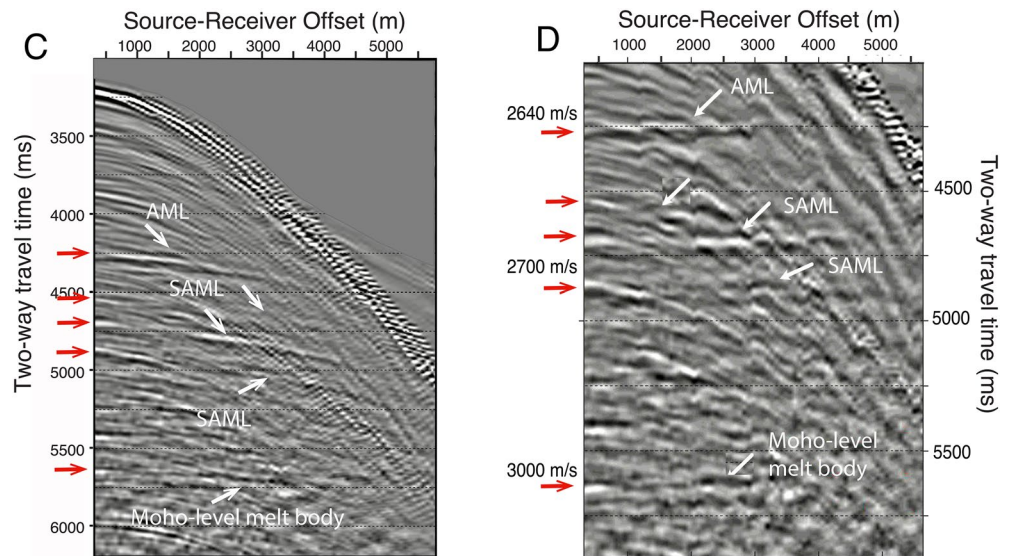
Figure 3. *Continued*

3.2. Other Crustal, Moho, and Near-Moho Reflections

Roughly 7.5 km south of the apex of Split Seamount, a Moho reflection is identified beneath the ridge axis deepening to the south at ∼2,200–2,400 ms below seafloor, and extending for ∼8 km (from CMP 4550 to 5800) in a region where an AML reflection is not detected in the crust above (Figures 3a and 3b). Directly beneath the center of Split Seamount, a narrow deep event at a similar twtt of 2,420 ms beneath seafloor is imaged, but in this location, a bright AML and series of SAML events are detected in the mid-crust above. This deep Moho-level reflection is a notably sharper, higher frequency event compared with the Moho event to the south, and in the stacked section, has broad edge diffractions (Figure 3b) inconsistent with an origin due to out-of-plane scattering from the seafloor. The edge diffractions indicate the presence of a finite body of limited extent with abrupt changes in physical properties at its edges; such diffractions are not typically observed from Moho reflections. Figures 3c and 3d show an example pre-stack super-CMP from near the apex of Split Seamount illustrating the Moho-level reflection event which is traceable to far offsets and with high moveout velocities that are consistent with reflections from the base of the crust. We interpret this reflection as arising from a Moho-level magma body, which, based on the migrated section (Figure 3b) has a lateral extent of ∼0.35 km.

Also, beneath Split Seamount, a prominent discontinuous event is detected, which transects the crust and dips to the north (Figure 3). At depth, this event crosses and extends below the Moho-level magma body. At shallow levels, it projects to the seafloor at ∼ CMP 4600 intersecting the trace of a small fault scarp detected in seafloor bathymetry that is oriented oblique to the ridge axis trending ∼45° (Figure 1c). This fault is one of a series of oblique trending scarps that transect the seafloor, reflecting rotated crust within the shear zone between Endeavor and Northern Symmetric segments due to the recent northward propagation of North Symmetric segment (Shoberg et al., 1991). We interpret the dipping intra-crustal event in our seismic section as the subsurface trace of one of these faults that transect the shear zone crust. Assuming the orientation of these fault scarps at the seafloor represents the true strike of the fault detected in our 2-D seismic section, the 28°–30° dip of the fault estimated at depth (assuming a range of velocities of 6.0–6.5 km/s in the on-axis lower crust) along our seismic line will underestimate the true dip (37°–39°). Other short events with similar dip are also found in the upper crust beneath Split Seamount and could be similar traces of pre-existing crustal faults, perhaps reactivated during the most recent phase (since 0.1 Ma) of extension and northward propagation of Northern Symmetric segment.

In addition to the Moho reflection detected south of Split Seamount, a possible faint Moho reflection is evident to the north of Split Seamount (Figure 3) and for short lengths beneath Endeavor segment (Figure 6 and S6). A cluster of deep events are detected at the southern end of Cleft segment at two-way travel times of
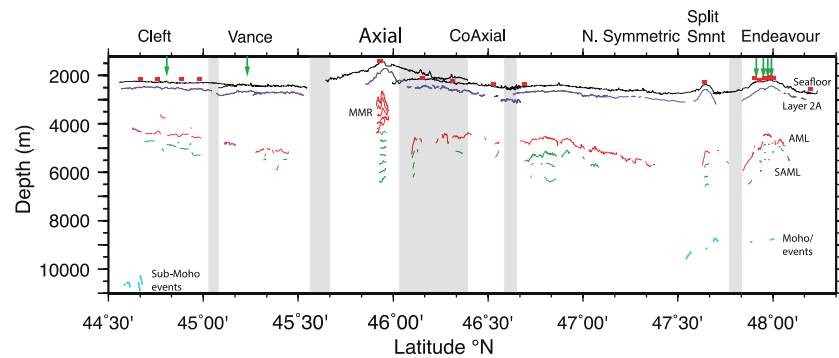
Figure 4. Axial structure along the JdF Ridge from along-axis seismic profiles including locations of the SAML events. Along-axis profile showing depth to seafloor (black), base of layer 2A (blue), AML (red/purple), SAML bodies (green), and Moho/sub-Moho events (cyan). Red rectangles indicate location of hydrothermal vents shown in Figure 1. Except for Axial Seamount, depths are calculated from reflection traveltimes using interval velocities of 2.65 km/s for layer 2A, 5.5 km/s for layer 2B and mid crust SAML and 6.5 km/s below. For Axial Seamount, magma reservoir picks are from seismic depth sections published in Carbotte et al. (2020; line 48) with depth to the top and bottom of the MMR shown in mid-weight red line with possible magma lens reflections within the MMR in fine red line. For the southern Cleft and Vance segments, we use the previously published AML interpretation (shown in purple) from Canales et al. (2006) which were derived from additional more-axially centered seismic lines acquired within these regions. Gray shaded rectangles indicate boundaries of the primary spreading segments along the JdF Ridge. Green arrows show locations of finer-scale (third order) segment boundaries that have been identified along several of the primary spreading segments.

2,200–2,800 ms below seafloor (Figure S2); we interpret these events as possible small magma bodies within the Moho transition zone and extending into uppermost mantle in this region.

4. Discussion

4.1. Comparisons With Other Mid-Ocean Ridge Sites and Implications for Magma Replenishment and Hydrothermal Venting

4.1.1. Comparisons With Stacked Magma Lenses Imaged at the EPR

Prior MOR studies have detected vertically stacked magma lenses in areas of higher mantle melt flux, including the fast spreading EPR (Arnulf, Singh, & Pye, 2014; Marjanović et al., 2014, 2018), the hotspot-influenced portion of the GSC (Boddupalli & Canales, 2019), and at Axial Seamount, which is an on-axis hotspot volcano at the JdF Ridge (Carbotte et al., 2020). In our new study, similar groups of magma lenses beneath the AML are detected along portions of each of the surveyed primary spreading segments of the JdF Ridge (Figure 4), indicating that these magma bodies also develop at the lower time-averaged melt flux conditions of this intermediate spreading ridge away from the hotpot. Some properties of the sub-AML lenses detected beneath the JdF Ridge differ from the faster spreading EPR, consistent with lower magma flux rates at slower spreading. Both the AML and SAML events are detected beneath less of the ridge axis at the JdF Ridge, 58% and 20% of the length of the axis, respectively (Figure 4), compared with detection levels of 85% and 35% for the EPR 8°20-10°10′N (Marjanović et al., 2018) and the overall ratio of SAML to AML incidence is lower (34% compared with 41% at the EPR). However, other characteristics of the sub-AML lenses are very similar at both ridges. The shallowest SAML reflections are found at ~100–800 m beneath the AML along the EPR, and these events are imaged at a similar depth range of 100–1,200 m along the JdF Ridge (Figure 5a). At both ridges, the SAML reflections are discontinuous quasi-horizontal events that extend for similar lengths of ~1–8 km along the axis (Figure 5b). Analysis of the high-resolution swath 3-D MCS dataset available for the EPR from 9°20-10°N indicates that the segmentation of these deeper magma lenses coincides with that of the AML above and punctuated sites of magma delivery through the crust at a spacing defined by the magma body segmentation is inferred (Marjanović et al., 2018).

With the lower resolution and sparse coverage provided by the available 2-D MCS data from the JdF Ridge, magmatic segmentation along this ridge is not well defined, and relationships between AML and SAML
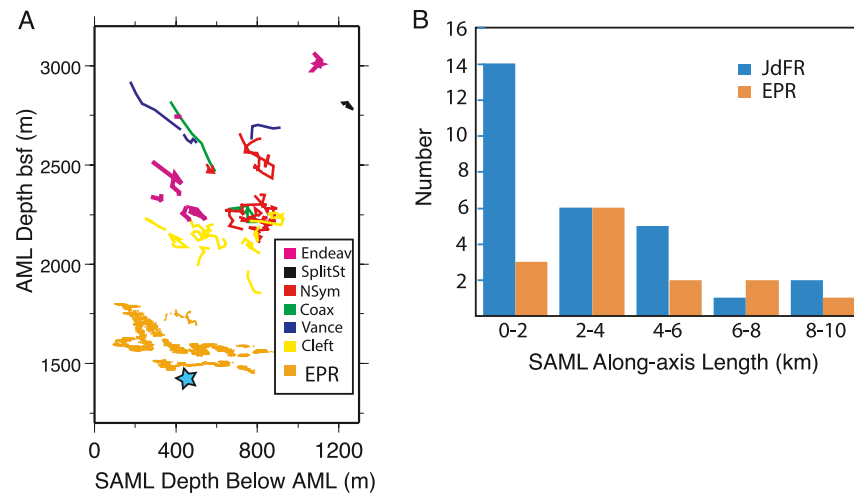
Figure 5. Comparison of AML and SAML properties at the JdF Ridge and the EPR 9°20-10°05′N. (a) Scatterplots showing AML and SAML depth below seafloor in meters for primary spreading segments of JdF Ridge (color-code shown in legend) and EPR using same crustal velocities for both ridge regions of 5.5 km/s for depth conversion of SAML events (see text). Data for only the shallowest SAML events from both ridges are shown. The spatial extents of the primary spreading segments of the JdF Ridge are indicated in Figure 4. Cyan star corresponds with average depth to the top of the MMR and to the first lens reflection beneath MMR base at Axial Seamount. (b) Histograms comparing along-axis lengths of shallowest SAML at both ridges. Data for the EPR are from Marjanović et al. (2018).

characteristics can only be examined for the larger scale tectonic segmentation of this ridge (e.g., Figures 4 and 5a). However, visual inspection suggests alignment of AML and deeper magma bodies beneath the fine-scale (third-order) segments defined at Endeavor Segment, consistent with the hypothesis of punctuated sites of deeper melt delivery below (Figures 4 and S6). Observations from Split Seamount of a narrow ~0.35 km Moho-level magma body centered directly beneath a broader region of stacked reflections (Figure 3) provide more direct evidence that these mid-crust magma lenses are fed from localized sites of melt delivery at the base of the crust. The along-axis extent of the AML and underlying magma lenses at Split Seamount is much greater (8–15 times) than that of the Moho-level magma body that we interpret as a local site of magma injection into the crust from the broader ~15 km in diameter region of high melt content that is estimated from the bulls-eye shaped low velocity zone detected in the uppermost mantle in this region (Arnoux et al., 2019).

4.1.2. Stacked Magma Lenses Coincide With Sites of Active/Enhanced Replenishment and Hydrothermal Venting

At Axial Seamount, observations from co-located long-term monitoring experiments are available (Chadwick et al., 2012; Nooner & Chadwick, 2016) and indicate that active magma replenishment is ongoing within regions where stacked magma lenses are imaged (Carbotte et al., 2020). The sill-like magma bodies detected at Axial Seamount form a narrow quasi-vertical conduit extending into the middle of the ~11 km thick crust beneath the broader shallow MMR that underlies the full extent of Axial caldera. This magma lens conduit is located near the best-fit inflation source determined from geodetic data, which corresponds with a near-vertical pipe-like body (Hefner et al., 2020; Nooner & Chadwick, 2016), and active magma replenishment via porous flow is inferred to be occurring within this region. The only other site on a MOR where active inflation has been documented to date is on the northern EPR where geodetic observations indicate an inflation source centered at 9°51′N that is located below the AML (Nooner et al., 2014). Magma lenses beneath the AML are detected in the area of this sub-AML inflation source (Marjanović et al., 2014, 2018), where inflation rates measured over a 3-year period are greater than expected given regional spreading rates, indicating enhanced magma replenishment at present. Within our study area at Endeavor segment, SAML events are detected beneath the AML in a region from ~47°57′-58′N (Figures 4 and S6) where seismicity associated with deeper magma injection is detected, indicating that this is also a site of active magma replenishment (Wilcock et al., 2009). It is noteworthy that in all ridge settings where magma lenses beneath
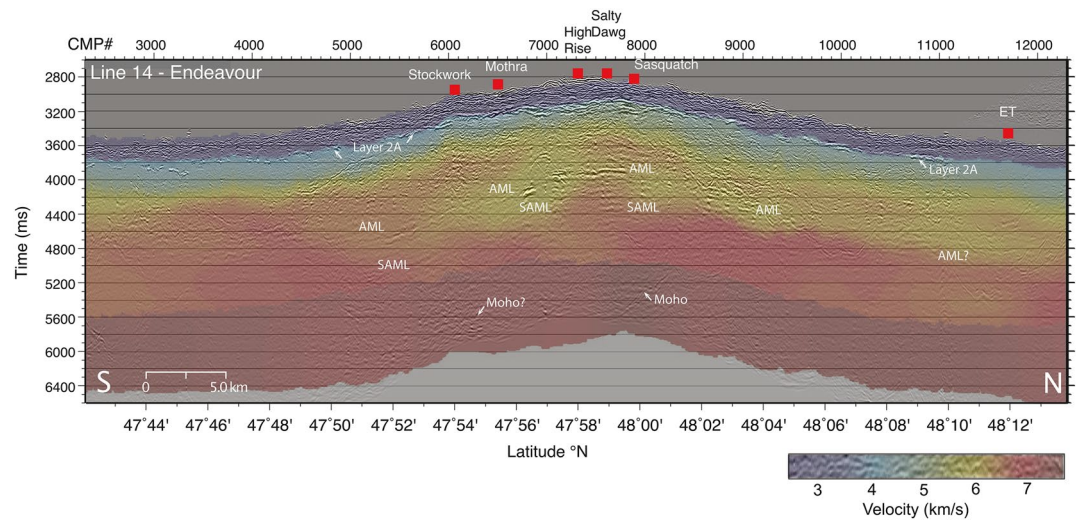
Figure 6. Comparison between MCS image from Endeavor segment and the tomography-derived velocity model of Arnoux et al. (2019). Along-axis seismic image is shown with the velocity model superimposed as a semi-transparent overlay. The velocity model is presented in two-way travel time and obtained by a simple depth to time conversion using tomography derived velocity and depth below seafloor at each grid point. Note the good alignment between the structure of the upper to mid crust in the tomography model and reflection section. The transition from low velocities in the shallowest crust to >4.5 km/s coincides with the base of layer 2A event in the MCS section. North of 47°52′N a prominent region of lower seismic velocities (5.7–6.5 km/s) in the mid-crust is present which coincides well with the region where AML and SAML reflections are identified. Figure S6 shows the interpreted horizons as transparent overlays for reference.

the AML have been detected, these bodies are more spatially localized features than the AML above, and these differences in incidence cannot be simply attributed to resolution limitations. For example, at Axial Seamount, the broad $\sim 14 \times 3$ km^2 and 0.5–1 km thick MMR beneath the caldera is thickest (and hence seismic penetration should be most limited) directly above the site where the localized ~ 3–5 km wide conduit of multiple deep magma lenses is detected (Carbotte et al., 2020). If stacked sub-axial magma lenses typically mark sites of active deep melt flux, an important inference is that the length of ridge undergoing significant magma replenishment at present is a small fraction of the total length of the ridge axis (20% at the JdF Ridge and 35% at the EPR inferred from SAML incidence along these ridges). Elsewhere along the ridge melt replenishment may be ongoing but at lower levels where SAML that can be detected with our seismic imaging do not form.

Previous studies of the distribution of hydrothermal venting along MOR suggest that active and possibly enhanced magma replenishment, beyond that needed to maintain seafloor spreading may be required to sustain high-temperature hydrothermal venting (e.g., Baker, 2009; Liu & Lowell, 2009; Lowell & Germanovich, 1994). A compilation of hydrothermal plume incidence and AML presence along over 2,100 km of fast and intermediate spreading ridges shows that while there is a strong correlation between venting location and presence of an AML, hydrothermal plumes are found along only a small fraction of the ridge length where an AML is detected (Baker, 2009). Baker speculates that the presence of the AML may be "a necessary but not sufficient" condition for venting and that active or enhanced magma replenishment may be needed to sustain high temperature hydrothermal venting, consistent with the thermal models of Liu and Lowell (2009). Interestingly, Baker (2009) reports plume incidence per ridge km along the JdF Ridge and EPR of 0.18 and 0.42, respectively, close to our estimates of SAML abundance along these ridges. Direct comparisons of the known seafloor vent sites along the JdF Ridge with SAML locations shows that of the few high-temperature hydrothermal sites identified along this ridge, most (14 out of 18) are found within regions where SAMLs are detected directly beneath or nearby (within 1 km) in the subsurface (Figures 1, 4, and S2–S6). These relationships lend further support to the hypothesis that locations of high temperature hydrothermal venting are sites of active and enhanced magma replenishment from below.
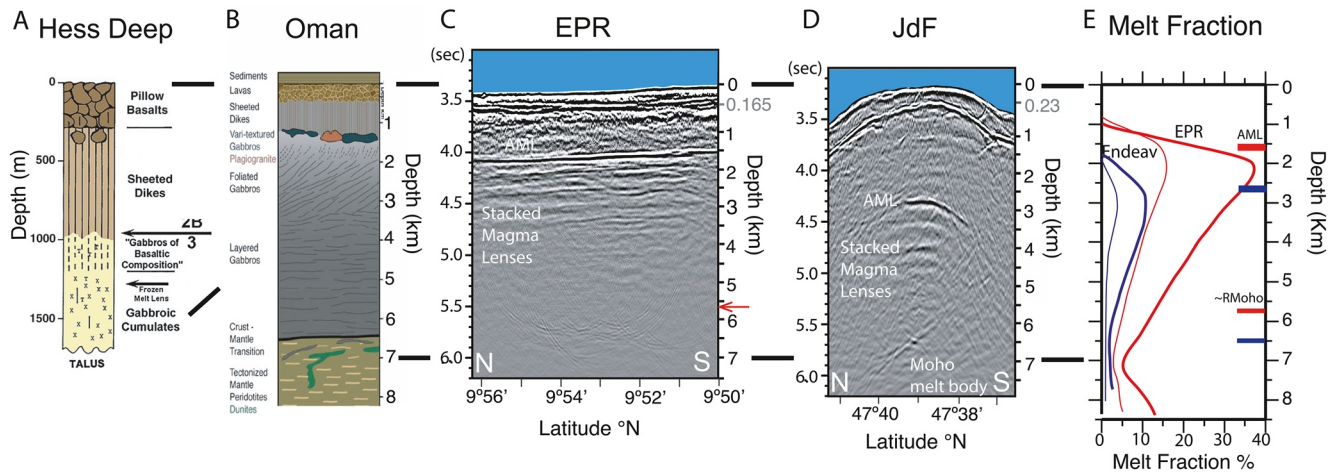
Figure 7. Comparison of seismic images and melt fraction estimates from the JdF Ridge and EPR with lithologic structure of oceanic crust from geologic exposures. (a) Schematic lithologic summary for the upper 1500 m of fast spreading oceanic crust derived from near-bottom observations at Hess Deep (from Natland & Dick, 2009). (b) Schematic lithologic summary of the Oman ophiolite (from Kelemen et al., 2014). (c) Along-axis seismic section from EPR (from Marjanović et al., 2018). Depth axis is estimated using interval velocity model at 9°50′N (2.26 km/s for layer 2A to depth value in gray and 5.5 km/s below) with 0 km corresponding to seafloor depth of 2500 m. Arrow on depth axis indicates approximate Moho depth below seafloor in this region derived from 3D pre-stack depth migrated data (from Boulahanis et al., 2020). (d) Along-axis seismic section from Split Seamount section of JdF Ridge. Depth axis is estimated using interval velocity model at 47°39′N (2.65 km/s for layer 2A to depth value in gray and 5.5 km/s below) with 0 km corresponding to seafloor depth of 2500 m. Arrow on depth axis indicates Moho depth inferred from reflection data. (e) Estimates of melt fraction through the crust and uppermost mantle at the ridge axis derived from seismic tomography studies of the EPR at ~9°30′N from Dunn et al. (2000) and of the Endeavor segment from Arnoux et al. (2019). EPR profiles are extracted from Vp profiles centered on ridge axis at 9°31.74′N shown in Dunn et al. (2000) using thermal models that account for anharmonic effects and calculated for melt residing in spheroids (thick red line) and in films (thin red line). Endeavor profiles are extracted for location of Main Endeavor hydrothermal field and are calculated assuming anelastic and anharmonic effects with melt residing in tubules and in films (thick and thin blue line respectively). Both studies use same assumptions for case of melt residing in films and different but comparable assumptions for the large aspect ratio case. Horizontal bars show location of the AML in seismic reflection sections at these same locations, and depth of reflection Moho (RMoho) from nearby locations (for the EPR 9°40′N from Boulahanis et al. (2020) and from Split Seamount panel (d)). All panels are aligned with top of oceanic crust at 0 km and all use same vertical scale except for the Hess Deep schematic (limited to the upper 1.7 km of the crust). Horizontal bars between panels indicate 0 and 7 km.

4.2. Relationship of Stacked Magma Lenses to Other Observations of Ridge Axis Seismic Structure

The SAML events imaged to date at both the JdF Ridge and EPR are detected ~1–2 km below the AML and do not extend to the base of the ~6–7 km thick crust formed in these regions. An important question is whether the lack of deeper reflection events reflects the true absence of deeper magma accumulations rather than an artifact of diminished resolution due to the effects of seismic attenuation and/or acquisition limitations. With the high seismic attenuation measured in the axial zone (Wilcock et al., 1992, 1995), the dominant wavelength of our imaging seismic source is expected to shift to lower frequencies with increasing depth, and magma bodies similar in thickness to those we identify in the mid-crust should become more difficult to detect in the lowermost crust. The sparse and 2-D acquisition of the available data from the JdF Ridge will also limit data resolution (e.g., Aghaei et al., 2014).

However, several lines of evidence, including from the MCS data, support the inference that the concentration of magma body reflections within the mid-crust reflects a true depth difference in the presence and/or size of magma accumulations. First, the presence of a bright reflection from the Moho-level magma body beneath Split Seamount (Figure 3), beneath a region where multiple magma lenses are imaged in the mid-crust, indicates that the extent of attenuation of the seismic imaging source through the lowermost crust does not preclude detecting structures at the base of the crust. The finding of deep lower crustal melt in the near axis region of Cleft segment (Canales et al., 2009) also supports the interpretation that deeper magma bodies, if present, can be detected within the axial zone.

Observations of seismic compressional wave (Vp) structure from seismic tomography and of shear wave velocity (Vs) structure derived from seafloor compliance measurements are available for portions of the JdF Ridge and EPR where our MCS studies are located (Arnoux et al., 2019; Dunn et al., 2000; Zha et al., 2014) and also indicate melt concentrations are higher in the mid-crust. At Endeavor segment a recent extensive
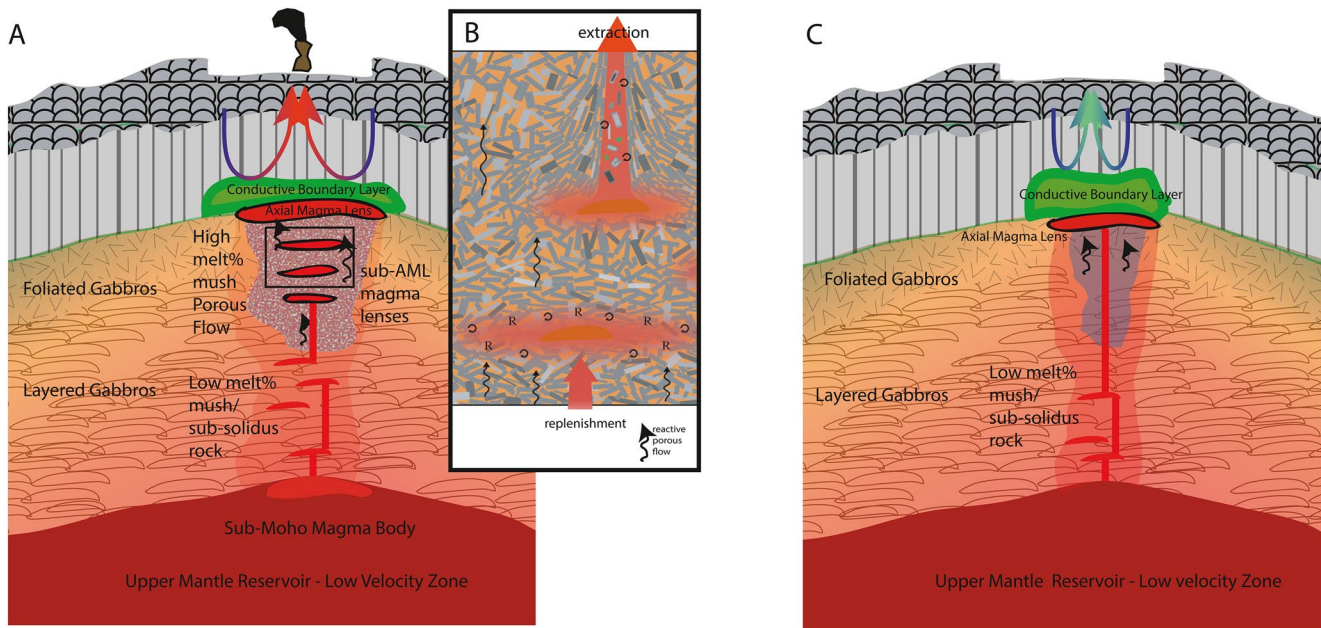
Figure 8. Schematic model of ridge-axis magmatic system derived from synthesis of geologic and geophysical observations. (a) At mid-ocean ridge sites during periods of enhanced magma replenishment, magma bodies may segregate from the uppermost mantle reservoir and accumulate at the base of the axial crust. Small magma lenses are emplaced in the lower crust (red) into hot partially solid rock with low percent of distributed melt forming the lower layered gabbros. Melts are expelled from the crystallizing lower crustal magma sills through small dikes to rise and accumulate in the mid-crust forming the higher melt content mush where the larger sub-AML bodies are focused (black outlined magma lenses). These mid-crust magma lenses, which are detectable in our MCS images, may typically be an order of magnitude thicker than the magma intrusions that form most of the lower layered gabbros. Reactive porous flow dominates in this part of the system and magma lenses may develop in this region via mush compaction. Pooling and accumulation of magmas beneath a thermally controlled permeability boundary at the base of the dike section contributes to the formation of the shallowest magma lens (labeled Axial Magma Lens) which is a longer-lived and more pervasive magma body than the deeper SAML. A conductive boundary layer separates the AML from hydrothermal fluid circulation in the dike and lava section above. Vigorous hydrothermal flow driven by sustained magma replenishment leads to development of high temperature hydrothermal venting at the seafloor. Black box delineates area of schematic in part (b). (b) Magma bodies beneath the axial magma lens may be rapidly drained during the dike intrusions and eruption events that build the upper crust, contributing to the vertical alignment of crystal fabrics and leaving little record of their horizontal orientations preserved within the foliated gabbros which dominate the upper part of the gabbro section (figure modified from Lissenberg et al., 2019). (c) In regions and time periods of reduced magma delivery to the crust, fewer magma intrusions are present in the lower crust, a narrower mush zone develops with lower melt fractions in the mid-crust and magma segregations large enough to be seismically imaged beneath the AML do not form. A thicker conductive boundary layer forms above the AML with weaker hydrothermal circulation in the upper crust and no high temperature hydrothermal venting at the seafloor (see text for further discussion).

seismic tomography study reveals a near continuous zone of low compressional velocities within the mid-crust that is ~5 km wide and narrowly focused along the ridge axis (Arnoux et al., 2019), with lowest Vp in the region where the AML and SAML events imaged in our data are located (Figure 6). Maximum inferred melt contents within this region are 1%–12% depending on assumed melt geometry and on whether ane-lasticity effects are included (Figure 7). Higher melt fractions in the mid-crust are also found at the EPR 9°30-35′N from a similar seismic tomography study (~5%–30% depending on model assumptions; Dunn et al., 2000, Figure 7). Similar results are found at the GSC where coincident MCS and tomography studies have been conducted. Here, the sub-AML bodies identified in MCS images are located within the depth range where the co-located tomography-derived crustal low velocity zone is most prominent and inter-preted as a mush reservoir containing up to 7% melt (Boddupalli & Canales, 2019; Canales et al., 2014). In all these regions, compressional velocities increase rapidly with depth suggesting melt fractions in the lowermost portion of the crust are lower, although velocity anomalies in this region will tend to be under-estimated due to more limited ray coverage.

Observations of seafloor compliance derived Vs structure are available for the same EPR region as the tomography studies and also indicate depth variations in the distribution of melt in the crust (Zha et al., 2014). These measurements are less affected by diffraction and attenuation effects in melt-rich zones

compared with the higher frequency body waves used for active source tomography. From the 3-D analysis of seafloor compliance data, Zha et al. (2014) infer a large 5–7 km wide low velocity zone in the mid-crust below the AML (depths from 1.5 to 4 km below seafloor) with maximum melt fractions of 5%–25% depending on melt geometry. Below this zone a narrower (4 km wide) low velocity zone in the lowermost crust (4–7 km below seafloor) is found that is inferred to be less continuous beneath the ridge axis than the mid-crust low velocity zone below the AML. While existing tomography and compliance studies at MOR are few, the available studies are consistent in finding that melt content within the crust varies with depth and is highest in the mid-crust region where the SAML events detected in seismic reflection studies are located.

4.3. Implications for the Origin of Sill-Like Magma Lenses Within the Mush Zone Beneath the AML

The origin of the AML detected beneath fast and intermediate ridges is commonly attributed to the presence of a thermally controlled permeability boundary located at the base of the upper crustal dike and lava section below which rising melts pond and accumulate. First-order variations are observed in the depth of the AML with spreading rate which are consistent with predictions of simple models of crustal formation whereby heat/melt delivery from the mantle due to spreading is balanced by heat removed by hydrothermal cooling, and provide strong support for this model (e.g., Chen & Lin, 2004; Hooft & Detrick, 1993; Phipps Morgan & Chen, 1993). A number of observations indicate that the sub-AML bodies develop under different conditions of formation from the AML. While these spatially more intermittent magma lenses are similar sub-horizontal and likely thin magma sills, they show no similar systematics in depth with spreading rate. The SAML are found at the same range of depths at the EPR and JdF Ridge whereas the overlying AML differs by up to 1 km in depth (Figure 5a), indicating that these magma bodies must be insulated from the strong thermal gradients in the crustal lid above the AML associated with hydrothermal cooling (e.g., Gillis, 2008). Given that the SAML are detected beneath only a fraction of the ridge length where the AML is present (Figure 4), higher magma flux conditions in excess of that needed to maintain the near-steady state AML are required. The SAML are also narrower than the AML above (Carbotte et al., 2020; Marjanović et al., 2018) and conditions of melt pooling below a permeability boundary that contribute to AML formation are inferred to allow for a wider magma lens to accumulate at the shallowest levels (Han et al., 2014).

There are a number of processes that can contribute to formation of sill-like magma bodies in magmatic systems. In the extensional stress regime of MORs where σ_3 is horizontal, regional stress conditions favor magma intrusions in vertical dikes rather than horizontal sills. Other possible mechanisms for the formation of horizontal magma lenses include the presence of compositional or rheological boundaries (e.g., Menand, 2008; 2011; Miller et al., 2011; Taisne & Jaupart, 2009). Mush bulk viscosities are expected to vary over several orders of magnitude from 10^{14} to 10^{18} Pa s depending on melt fraction and temperature, and it is possible that rheological boundaries between strong and weaker mush zones could act to arrest rising melts from below causing formation of magma accumulations (Sparks et al., 2019). Magma layers may develop from conversion of mush as a result of heating during replenishment events with intrusion of, for example, hotter more primitive magma from below (e.g., Huppert & Sparks, 1988; Sparks et al., 2019). For a sill-like magma body forming in a strong mush or near solid matrix, deeper rising melts would be expected to be trapped at this level with further upward migration of melt impeded until the strength of the overlying roof matrix is exceeded. An alternate mechanism is melt segregation from a mush via compaction, which is predicted to give rise to quasi-regular spaced melt accumulations or porosity waves (Jackson et al., 2018; McKenzie, 1984; Spiegelman, 1993a, 1993b). Carbotte et al. (2020) interpret the series of vertically stacked magma lenses detected beneath Axial Seamount as similar mush compaction features based on numerical modeling, observations of lens spacing, and colocation with the deep conduit where active porous flow is inferred from long-term geodetic measurements of volcano inflation (Hefner et al., 2020; Nooner & Chadwick, 2016). Given these findings, our favored interpretation for the similar stacked magma lenses detected beneath the JdF Ridge and elsewhere beneath MORs, which locate in the most melt rich portion of the axial crust, in locations where other observations support active melt replenishment, as melt segregations due to compaction of a mush undergoing porous flow (Figure 8). We expect, however, that multiple processes contribute to the development of magma ac-

cumulations within the crustal accretion zone as magma replenishment waxes and wanes through time. Mush compaction in the sub-AML region may be a more important process during periods of enhanced magma flux from depth when a wider and perhaps higher melt content mush zone in the mid-crust develops whereas during lower magma flux phases, melt transport throughout the crust may be more dominated by dike intrusion (Figures 8a and 8c).

4.4. Geologic Constraints and Synthesis of Observations on the Formation of the Gabbroic Section of the Crust

The SAML events detected to date at MOR are from fast and magma-rich intermediate spreading ridges. Assuming that the AML at these ridges resides at the approximate dike-to-gabbro transition (e.g., Phipps Morgan & Chen, 1993; Sinton & Detrick, 1992), the SAML events locate within the upper part of the gabbro section. Geologic constraints on the formation of the gabbroic crust at these spreading rates are sparse and are primarily from *in situ* seafloor observations of EPR crust exposed in two locations, at Hess and Pito deeps, as well as studies of the Oman ophiolite, inferred to have formed at a fast-spreading ridge (Figure 7). These studies reveal high variability over short distances but support a generalized plutonic crust composed of an upper section of varitextured/isotropic and subvertically foliated gabbros and a deeper section of horizontally layered gabbros (e.g., Boudier et al., 1996; Brown et al., 2019; Gillis et al., 2014; Karson et al., 2015; Koepke et al., 2020; MacLeod & Yaouancq, 2000; Natland & Dick, 2009; Nicolas et al., 1988; VanTongeren et al., 2008). Recent mapping and sampling of seafloor fault exposures at Pito Deep provides direct observations of the upper ~1 km of the gabbro section where depths relative to the overlying dike section are well constrained. This upper gabbro section includes a <100 m layer of varitextured gabbros overlying ~0.5–1 km of foliated gabbros (Brown et al., 2019). The varitextured gabbros sampled are characterized by more evolved compositions, distinct textures and minor amounts of intercrystalline strain and are interpreted to have formed within the paleo-AML. The foliated gabbros are characterized by steepening to near vertical fabrics, are more primitive in composition, record increasing amounts of intercrystalline strain down section and are interpreted to form in the crystal mush beneath the AML (Brown et al., 2019). The origin of the steep fabrics of the foliated gabbros is the subject of ongoing debate, with early gabbro glacier and hybrid models for lower crustal formation, as well as the recent observations from Pito Deep, attributing the steeply dipping fabrics to subsidence and rotation of cumulate material formed within the AML into the underlying mush (Boudier et al., 1996; Brown et al., 2019; Nicolas et al., 1988; Phipps Morgan & Chen, 1993). In other studies, these fabrics are attributed to buoyant ascent of melts through the mush, possibly via porous flow, or to more focused vertical transport of melts through channels or dikes with little vertical transport of the crystalline matrix (Lissenberg et al., 2004, 2013; MacLeod & Yaouancq, 2000).

These geologic observations of *in situ* exposures, supported by observations from the Oman ophiolite (MacLeod & Yaouancq, 2000; Nicolas et al., 2009), suggest that gabbros at the stratigraphic level of the AML and sub-AML differ, consistent with our interpretations that the conditions of formation for these sill-like magma bodies are different. The subhorizontal magma lenses that we observe range from ~100 to 1,200 m below the AML are in the region of highest melt content inferred from seismic tomography studies, and span the foliated gabbro section in exposures of oceanic crust, where steep to near vertical, not horizontal, fabrics are found. That evidence for these magma lenses is not preserved within the available observations from the shallow gabbros may reflect efficient drainage of melts from the shallow part of the mush zone during MOR dike intrusion and eruption events. Support for this interpretation comes from observations of a prominent gap in the shallowest SAML reflections with evidence for seismic velocity pull-up of deeper horizons beneath the source region of the 2006 eruption at the EPR ~9°50′N and which Marjanović et al. (2014) attribute to melt draining associated with the 2006 eruption. From their time-series measurements of seafloor compliance in this same region, Zha et al. (2014) also find evidence for less melt in the crustal low-velocity zone after the 2006 eruption, which they attribute to eruption-related melt drainage below the AML. We speculate that rapid extraction of magma from the SAMLs detected beneath the AML during eruptions contributes to the steepening to vertical foliations and the intercrystalline strain documented (Brown et al., 2019) within the upper gabbros at Pito Deep.

While the available studies of seafloor exposures at Pito and Hess Deeps provide good constraints, although spatially limited, on the upper gabbros of fast-spread crust, geologic information on the structure of deeper gabbros, where the stratigraphic position within the crust can be well constrained, is derived primarily from observations of the Oman ophiolite (Figure 7). The modally layered gabbros of the lowermost crust exposed in Oman are characterized by shallowly dipping foliations oriented sub-parallel to paleo-Moho (Boudier et al., 1996; Pallister & Hopson, 1981). The prevailing model for the formation of these layered gabbros is via *in situ* crystallization of magmas within a series of thin sills embedded within what is inferred to be subsolidus country rocks (Kelemen et al., 1997; Korenaga & Kelemen, 1997). The deeper magma lenses we image extend to depths of the upper layered gabbros in ophiolite exposures and in previous studies the SAML are interpreted to be the shallowest-level examples of these lower crustal sills prior to crystallization (Marjanović et al., 2014). The estimated thickness of the magma source bodies for the layered gabbros is of the order of 10 s of m or less (Korenaga & Kelemen, 1997), which is thinner than is likely to be resolvable with our MCS data and the lack of pervasive SAML reflections extending throughout the deep crust in our data set does not preclude their presence. Indeed, there are other seismic observations that support the presence of horizontally aligned magma bodies within the lower crust.

For example, from their compliance study of the EPR, Zha et al. (2014) infer Vs/Vp ratios in the axial lower crust that are consistent with melt in low aspect ratio horizontally aligned cracks or sills analogous to the decimeter sills of Oman. Other indirect indications of significant Vp anisotropy in axial lower crust related to sub-horizontal alignment come from discrepancies in estimates of crustal thickness in the ridge axis region obtained with reflection imaging compared with tomography-based estimates. At the EPR 9°30′-55′N, near-axis crustal thickness derived from tomography studies, which make use of seismic phases traveling sub-horizontally through the crust, are ∼1 km thicker than obtained from colocated pre-stack time migrated (PSTM) MCS data, which makes use of near-vertical incident phases and crustal velocities derived from the PSTM analysis (Figure 7; Aghaei et al., 2014; Canales et al., 2003; Dunn et al., 2000; Marjanović et al., 2018). Similar differences of ∼1–0.75 km are noted at the Endeavor segment (Figure 7; Arnoux et al., 2019) and at the GSC (Boddupalli & Canales, 2019) with thicker crust inferred from the tomography studies although in these cases lower crustal velocities are unconstrained from the reflection data. In the EPR case, where velocity constraints are derived from the MCS data, differences due to velocity uncertainties can be ruled out. Sub-horizontal layering of magma bodies should have a greater influence on near-vertical travel times than on the wide-angle travel times used in tomography studies (Hammond & Kendall, 2016). The nature of the inferred anisotropy, slower velocities in the vertical direction, is also consistent with the strong radial anisotropy in Vs detected at currently active subaerial volcanoes that has been attributed to the presence of horizontal magma accumulations (Jaxybulatov et al., 2014). Also of note, in old ∼ 70 Ma Pacific crust Russell et al. (2019) measure significant radial anisotropy in the lower crust (Vsh > Vsv) which they attributed to the signature of sub-horizontal layering in the gabbroic crust.

From compositions of the basalt and dike section at Oman, which are in Fe–Mg equilibrium with the cumulates of the layered gabbro section, as well as other observations of mineral compositions, Kelemen et al. (1997), and Korenaga and Kelemen (1998) infer transport of melts from the lower crustal magma bodies to shallow levels through vertical melt-filled cracks rather than via porous flow. Other observations suggest that reactive porous flow is an important process operating throughout the crust as expected for a mush dominated system (Lissenberg et al., 2013, 2019). Based on the existing seismic tomography data, we speculate that the high-melt content mush, where porous flow processes dominate, may be largely concentrated in the mid-crust region proximal to the AML. Given that most of the stacked magma lenses we have imaged to date locate in the more melt rich mid-crust region where geologic observations indicate sub-vertically foliated gabbros, our favored interpretation is that porous flow processes of mush compaction contribute to SAML formation (Figure 8). Magmas may be expelled from the thin lower crustal sills that form the deeper layered gabbros through small dikes to rise and accumulate in the mid-crust forming the higher melt content mush where the SAML are focused. These magma bodies are rapidly drained during the dike intrusions and eruption events that build the upper crust, contributing magmas to these events and leaving little record of their horizontal orientations preserved within the upper foliated gabbros of the crust.

5. Conclusions

The primary conclusions derived from our observations of stacked magma lenses beneath MOR and synthesis of other geophysical and geologic observations are:

1. Local sites of vertically stacked magma lenses are found beneath the AML along the intermediate spreading JdF Ridge, similar to those found at higher magma flux fast and hotspot-influenced ridges. Multi-level vertically stacked magma lens complexes underlie the majority of high temperature vent sites along the JdF Ridge and are inferred to mark local regions of melt delivery from the mantle, where evidence from long-term monitoring studies indicate active and possibly enhanced magma replenishment is occurring. From their low incidence per ridge km we infer that only a fraction of the ridge axis at present is in a phase of active magma replenishment;

2. Magma lenses detected beneath the AML in the currently available data are focused in the mid-crust, which coincides with the most melt rich part of the crystal mush zone detected in seismic tomography and compliance studies. *In situ* exposures of oceanic crust and ophiolites, which provide geologic constraints on the final products of crustal formation, show sub-vertical fabrics within the uppermost gabbros where most of the stacked magma lenses that have been imaged locate. We infer that the sub-horizontal multi-level magma bodies detected beneath the AML do not cool and crystallize *in situ* and that the steep fabrics preserved at this stratigraphic level reflect porous flow along with the effects of rapid melt extraction during dike intrusion and eruption events that drain magmas from the shallow sill-like magma lenses;

3. Different conditions of formation for the AML and underlying stacked magma lenses are inferred from the distribution and characteristics of these magma bodies. The AML, which is a more laterally pervasive and typically wider magma body, shows strong systematics in depth with spreading rate consistent with formation by melt pooling beneath a thermally controlled permeability boundary. The more intermittent and narrower lenses found below the AML show no similar systematics and appear to be insulated from effects of hydrothermal cooling above the AML. From evidence for their formation within the most melt rich portion of the axial crust and in locations where active melt replenishment from depth is inferred from seafloor geodetic studies, our favored interpretation is that compaction of mush undergoing porous flow contributes to the formation of the imaged melt segregations below the AML;

4. The vertically stacked magma lenses imaged to date are not found through the crust to the deepest sections where horizontally layered gabbros dominate in ophiolite exposures. The lack of reflections in the deepest crust could reflect imaging limitations such that the magma lenses that form the lower layered gabbro section are too thin to be imaged with our imaging source. Alternatively, given the positive buoyancy of melts and high overburden pressures at depth in the crust, residence times for melt within the lower crust is likely to be short. Perhaps only the shallowest of the layered gabbro intrusions persist as molten bodies for significant time periods and the magma lenses we image correspond to these, likely thicker, magma accumulations that form in the higher melt content mid crust.

Data Availability Statement

Data used in this study are archived and publicly available through the Marine Geoscience Data System (Carbotte et al., 2014; http://www.marine-geo.org/tools/search/entry.php?id=EW0207).

References

Aghaei, O., Nedimović, M. R., Carton, H., Carbotte, S. M., Canales, J. P., & Mutter, J. C. (2014). Crustal thickness and Moho character of the fast-spreading East Pacific Rise from 9°42′N to 9°57′N from poststack-migrated 3-D MCS data. *Geochemistry, Geophysics, Geosystems*, *15*(3), 634–657. https://doi.org/10.1002/2013gc005069

Arnoux, G. M., Toomey, D. R., Hooft, E. E. E., & Wilcock, W. S. D. (2019). Seismic imaging and physical properties of the Endeavor segment: Evidence that skew between mantle and crustal magmatic systems governs spreading center processes. *Geochemistry, Geophysics, Geosystems*, *20*, 1319–1339. https://doi.org/10.1029/2018gc007978

Arnulf, A. F., Harding, A. J., Kent, G. M., Carbotte, S. M., Canales, J. P., & Nedimović, M. R. (2014). Anatomy of an active submarine volcano. *Geology*, *42*, 655–658. https://doi.org/10.1130/g35629.1

Arnulf, A. F., Harding, A. J., Kent, G. M., & Wilcock, W. S. D. (2018). Structure, seismicity, and accretionary processes at the hot spot-influenced axial seamount on the Juan de Fuca Ridge. *Journal of Geophysical Research: Solid Earth*, *123*, 4618–4646. https://doi.org/10.1029/2017jb015131

Arnulf, A. F., Singh, S. C., & Pye, J. W. (2014). Seismic evidence of a complex multi-lens melt reservoir beneath the 9° N Overlapping Spreading Center at the East Pacific Rise. *Geophysical Research Letters*, *41*, 6109–6115. https://doi.org/10.1002/2014gl060859

Baker, E. T. (2009). Relationships between hydrothermal activity and axial magma chamber distribution, depth, and melt content. *Geochemistry, Geophysics, Geosystems*, *10*(6). https://doi.org/10.1029/2009gc002424

Beaulieu, S. E. & Szafrański, K. M. (2020). *InterRidge global database of active submarine hydrothermal vent fields version 3.4*. PANGAEA. https://doi.org/10.1594/PANGAEA.917894

Boddupalli, B., & Canales, J. P. (2019). Distribution of crustal melt bodies at the hot spot-influenced section of the Galápagos Spreading Centre from seismic reflection images. *Geophysical Research Letters*, *46*, 4664. https://doi.org/10.1029/2019gl082201

Boudier, F., Nicolas, A., & Ildefonse, B. (1996). Magma chambers in the Oman ophiolite: Fed from the top and the bottom. *Earth and Planetary Science Letters*, *144*(1–2), 239–250. https://doi.org/10.1016/0012-821x(96)00167-7

Boulahanis, B., Carbotte, S. M., Huybers, P. J., Nedimović, M. R., Aghaei, O., Canales, J. P., & Langmuir, C. H. (2020). Do sea level variations influence mid-ocean ridge magma supply? A test using crustal thickness and bathymetry data from the East Pacific Rise. *Earth and Planetary Science Letters*, *535*, 116121. https://doi.org/10.1016/j.epsl.2020.116121

Brown, T. C., Cheadle, M. J., John, B. E., Coogan, L. A., Gee, J. S., Karson, J. A., & Swapp, S. M. (2019). Textural character of gabbroic rocks from Pito Deep: A record of magmatic processes and the genesis of the upper plutonic crust at fast-spreading mid-ocean ridges. *Journal of Petrology*, *60*(5), 997–1026. https://doi.org/10.1093/petrology/egz022

Canales, J. P., Detrick, R. S., Carbotte, S. M., Kent, G. M., Diebold, J. B., Harding, A., et al. (2005). Upper crustal structure and axial topography at intermediate spreading ridges: Seismic constraints from the southern Juan de Fuca Ridge. *Journal of Geophysical Research*, *110*(B12). https://doi.org/10.1029/2005jb003630

Canales, J. P., Detrick, R. S., Toomey, D. R., & Wilcock, W. S. (2003). Segment-scale variations in the crustal structure of 150–300 kyr old fast spreading oceanic crust (East Pacific Rise, 8 15′ N–10 5′ N) from wide-angle seismic refraction profiles. *Geophysical Journal International*, *152*(3), 766–794.

Canales, J. P., Dunn, R. A., Ito, G., Detrick, R. S., & Sallarès, V. (2014). Effect of variations in magma supply on the crustal structure of mid-ocean ridges. *The Galapagos: A Natural Laboratory for the Earth Sciences*, *204*, 363. https://doi.org/10.1002/9781118852538.ch17

Canales, J. P., Nedimović, M. R., Kent, G. M., Carbotte, S. M., & Detrick, R. S. (2009). Seismic reflection images of a near-axis melt sill within the lower crust at the Juan de Fuca ridge. *Nature*, *460*(7251), 89–93. https://doi.org/10.1038/nature08095

Canales, J., Singh, S., Detrick, R., Carbotte, S., Harding, A., Kent, G., et al. (2006). Seismic evidence for variations in axial magma chamber properties along the southern Juan de Fuca Ridge. *Earth and Planetary Science Letters*, *246*, 353–366. https://doi.org/10.1016/j.epsl.2006.04.032

Carbotte, S., HardingKentCanales, A. G. J. P., & Nedimovic, M. (2014). Raw multi-channel Seismic Shot data from the Juan de Fuca Spreading Center acquired during the *R/V Maurice Ewing Expedition*, EW0207. https://doi.org/10.1594/IEDA/306864

Carbotte, S. M., Arnulf, A., Spiegelman, M., Lee, M., Harding, A., Kent, G., et al. (2020). Stacked sills forming a deep melt-mush feeder conduit beneath Axial Seamount. *Geology*, *48*. https://doi.org/10.1130/g47223.1

Carbotte, S. M., Detrick, R. S., Harding, A., Canales, J. P., Babcock, J., Kent, G., et al. (2006). Rift topography linked to magmatism at the intermediate spreading Juan de Fuca Ridge. *Geology*, *34*, 209–212. https://doi.org/10.1130/g21969.1

Carbotte, S. M., Nedimović, M. R., Canales, J. P., Kent, G. M., Harding, A. J., & Marjanović, M. (2008). Variable crustal structure along the Juan de Fuca Ridge: Influence of on-axis hot spots and absolute plate motions. *Geochemistry, Geophysics, Geosystems*, *9*(8). https://doi.org/10.1029/2007gc001922

Cashman, K. V., Sparks, R. S. J., & Blundy, J. D. (2017). Vertically extensive and unstable magmatic systems: A unified view of igneous processes. *Science*, *355*, 6331. https://doi.org/10.1126/science.aag3055

Chadwick, W. W., Jr, Nooner, S. L., Butterfield, D. A., & Lilley, M. D. (2012). Seafloor deformation and forecasts of the April 2011 eruption at Axial Seamount. *Nature Geoscience*, *5*, 474. https://doi.org/10.1038/ngeo1464

Chen, Y. J., & Lin, J. (2004). High sensitivity of ocean ridge thermal structure to changes in magma supply: The Galapagos Spreading Center. *Earth Planetary Science Letters*, *221*(1–4), 263–273. https://doi.org/10.1016/s0012-821x(04)00099-8

Coogan, L. A. (2014). *Treatise on geochemistry* (2nd ed., pp. 497–541). http://dx.doi.org/10.1016/B978-0-08-095975-7.00316-8. The lower oceanic crust.

Crawford, W. C., Webb, S. C., & Hildebrand, J. A. (1999). Constraints on melt in the lower crust and Moho at the East Pacific Rise, 9°48′N, using seafloor compliance measurements. *Journal of Geophysical Research*, *104*(B2), 2923–2939. https://doi.org/10.1029/1998jb900087

Detrick, R. S., Harding, A. J., Kent, G. M., Orcutt, J. A., Mutter, J. C., & Buhl, P. (1993). Seismic structure of the southern East Pacific Rise. *Science*, *259*(5094), 499–503. https://doi.org/10.1126/science.259.5094.499

Dunn, R. A., Toomey, D. R., & Solomon, S. C. (2000). Three-dimensional seismic structure and physical properties of the crust and shallow mantle beneath the East Pacific Rise at 9°30′N. *Journal of Geophysical Research*, *105*, 23537–23555. https://doi.org/10.1029/2000jb900210

Garmany, J. (1989). Accumulations of melt at the base of young oceanic crust. *Nature*, *340*(6235), 628–632. https://doi.org/10.1038/340628a0

Gillis, K. M. (2008). The roof of an axial magma chamber: A hornfelsic heat exchanger. *Geology*, *36*(4), 299–302. https://doi.org/10.1130/g24590a.1

Gillis, K. M., Snow, J. E., Klaus, A., Abe, N., Adrião, Á. B., Akizawa, N., et al. (2014). Primitive layered gabbros from fast-spreading lower oceanic crust. *Nature*, *505*(7482), 204–207. https://doi.org/10.1038/nature12778

Grove, T. L., Kinzler, R. J., & Bryan, W. B. (1992). Fractionation of mid-ocean ridge basalt (MORB). In *Mantle flow and melt generation at mid-ocean ridges*. AGU Monograph (pp. 281–310).

Hammond, J. O. S., & Kendall, J.-M. (2016). Constraints on melt distribution from seismology: A case study in Ethiopia. *Geological Society, London, Special Publications*, *420*(1), 127–147. https://doi.org/10.1144/sp420.14

Han, S., Carbotte, S. M., Carton, H., Mutter, J. C., Aghaei, O., Nedimović, M. R., & Canales, J. P. (2014). Architecture of on- and off-axis magma bodies at EPR 9°37-40′N and implications for oceanic crustal accretion. *Earth and Planetary Science Letters*, *390*, 31–44. https://doi.org/10.1016/j.epsl.2013.12.040

Hefner, W. L., Nooner, S. L., Chadwick, W. W., Jr., & Bohnenstiehl, D. R. (2020). Revised Magmatic Source Models for the 2015 Eruption at Axial Seamount including estimates of fault-induced deformation. *Journal of Geophysical Research*, *125*(4), e2020JB019356. https://doi.org/10.1029/2020jb019356

Henstock, T. J., Woods, A. W., & White, R. S. (1993). The accretion of oceanic crust by episodic sill intrusion. *Journal of Geophysical Research*, *98*(B3), 4143–4161. https://doi.org/10.1029/92jb02661

Hooft, E. E., & Detrick, R. S. (1993). The role of density in the accumulation of basaltic melts at mid-ocean ridges. *Geophysical Research Letters*, *20*(6), 423–426. https://doi.org/10.1029/93GL00295

Huppert, H. E., & Sparks, R. S. J. (1988). The generation of granitic magmas by intrusion of basalt into continental crust. *Journal of Petrology*, *29*(3), 599–624. https://doi.org/10.1093/petrology/29.3.599

Jackson, M. D., Blundy, J., & Sparks, R. S. J. (2018). Chemical differentiation, cold storage and remobilization of magma in the Earth's crust. *Nature*, *564*, 405. https://doi.org/10.1038/s41586-018-0746-2

Jaxybulatov, K., Shapiro, N. M., Koulakov, I., Mordret, A., Landes, M., & Sens-Schonfelder, C. (2014). A large magmatic sill complex beneath the Toba caldera. *Science*, *346*, 617–619. https://doi.org/10.1126/science.1258582

Karson, J. A., Kelley, D. S., Fornari, D. J., Perfit, M. R., & Shank, T. M. (2015). *Discovering the deep: A photographic atlas of the seafloor and oceanic crust*. Cambridge University Press.

Karson, J. A., Klein, E. M., Hurst, S. D., Lee, C. E., Rivizzigno, P. A., Curewitz, D., et al. (2002). Structure of uppermost fast-spread oceanic crust exposed at the Hess Deep Rift: Implications for subaxial processes at the East Pacific Rise. *Geochemistry, Geophysics, Geosystems*, *3*(1). https://doi.org/10.1029/2001gc000155

Kelemen, P. B., Koga, K., & Shimizu, N. (1997). Geochemistry of gabbro sills in the crust-mantle transition zone of the Oman ophiolite: Implications for the origin of the oceanic lower crust. *Earth and Planetary Science Letters*, *146*(3–4), 475–488. https://doi.org/10.1016/s0012-821x(96)00235-x

Kelemen, P. B., Matter, J. M., & Teagle, D. A. (2014). Scientific Drilling in the Samail Ophiolite, Sultanate of Oman. Unpublished proposal to the International Continental Drilling Program. Retrieved from http://www.ldeo.columbia.edu/gpg/projects/icdp-workshop-oman-drilling-project

Kent, G. M., Harding, A. J., Orcutt, J. A., Detrick, R. S., Mutter, J. C., & Buhl, P. (1994). Uniform accretion of oceanic crust south of the Garrett transform at 14°15′S on the East Pacific Rise. *Journal of Geophysical Research*, *99*, 9097–9116. https://doi.org/10.1029/93jb02872

Koepke, J., Garbe-Schoenberg, D., Mueller, T., Mueller, S., Mock, D., Schuth, S., & Ildefonse, B. (2020). *A reference section through the lower crust in the Wadi Gideah (Sumail ophiolite, Sultanate Oman): The crustal drill sites within the ICDP OmanDP and related work, Paper presented at 2020 International Conference on Ophiolites and the oceanic Lithosphere: Results of the Oman Drilling Project and related research, Muscat*.

Korenaga, J., & Kelemen, P. (1998). Melt migration through the oceanic lower crust: A constraint from melt percolation modeling with finite solid diffusion. *Earth and Planetary Science Letters*, *156*, 1–11. https://doi.org/10.1016/s0012-821x(98)00004-1

Korenaga, J., & Kelemen, P. B. (1997). Origin of gabbro sills in the Moho transition zone of the Oman ophiolite: Implications for magma transport in the oceanic lower crust. *Journal of Geophysical Research*, *102*(B12), 27729–27749. https://doi.org/10.1029/97jb02604

Lissenberg, C. J., Bedard, J. H., & van Staal, C. R. (2004). The structure and geochemistry of the gabbro zone of the Annieopsquotch ophiolite, Newfoundland: Implications for lower crustal accretion at spreading ridges. *Earth and Planetary Science Letters*, *229*(1–2), 105–123. https://doi.org/10.1016/j.epsl.2004.10.029

Lissenberg, C. J., MacLeod, C. J., & Bennett, E. N. (2019). Consequences of a crystal mush-dominated magma plumbing system: a mid-ocean ridge perspective. *Philosophical Transactions of the Royal Society of London A*, *377*(2139), 20180014. https://doi.org/10.1098/rsta.2018.0014

Lissenberg, C. J., MacLeod, C. J., Howard, K. A., & Godard, M. (2013). Pervasive reactive melt migration through fast-spreading lower oceanic crust (Hess Deep, equatorial Pacific Ocean). *Earth and Planetary Science Letters*, *361*, 436–447. https://doi.org/10.1016/j.epsl.2012.11.012

Liu, L., & Lowell, R. P. (2009). Models of hydrothermal heat output from a convecting, crystallizing, replenished magma chamber beneath an oceanic spreading center. *Journal of Geophysical Research*, *114*, B02102. https://doi.org/10.1029/2008JB005846

Lowell, R. P., & Germanovich, L. N. (1994). On the temporal evolution of high-temperature hydrothermal systems at ocean ridge crests. *Journal of Geophysical Research*, *99*, 565–575. https://doi.org/10.1029/93jb02568

Maclennan, J., Hulme, T., & Singh, S. C. (2004). Thermal models of oceanic crustal accretion: Linking geophysical, geological and petrological observations. *Geochemistry, Geophysics, Geosystems*, *5*(2). https://doi.org/10.1029/2003gc000605

MacLeod, C. J., & Yaouancq, G. (2000). A fossil melt lens in the Oman ophiolite: Implications for magma chamber processes at fast spreading ridges. *Earth and Planetary Science Letters*, *176*(3–4), 357–373. https://doi.org/10.1016/s0012-821x(00)00020-0

Marjanović, M., Carbotte, S. M., Carton, H. D., Nedimović, M. R., Canales, J. P., & Mutter, J. C. (2018). Crustal magmatic system beneath the East Pacific Rise (8° 20′ to 10° 10′ N): Implications for tectonomagmatic segmentation and crustal melt transport at fast-spreading ridges. *Geochemistry, Geophysics, Geosystems*, *19*(11), 4584–4611.

Marjanović, M., Carbotte, S. M., Carton, H., Nedimović, M. R., Mutter, J. C., & Canales, J. P. (2014). A multi-sill magma plumbing system beneath the axis of the East Pacific Rise. *Nature Geoscience*, *7*, 825.

McKenzie, D. (1984). The generation and compaction of partially molten rock. *Journal of Petrology*, *25*, 713–765. https://doi.org/10.1093/petrology/25.3.713

Menand, T. (2008). The mechanics and dynamics of sills in layered elastic rocks and their implications for the growth of laccoliths and other igneous complexes. *Earth and Planetary Science Letters*, *267*, 93–99. https://doi.org/10.1016/j.epsl.2007.11.043

Menand, T. (2011). Physical controls and depth of emplacement of igneous bodies: A review. *Tectonophysics*, *500*, 11–19. https://doi.org/10.1016/j.tecto.2009.10.016

Miller, C. F., Furbish, D. J., Walker, B. A., Claiborne, L. L., Koteas, G. C., Bleick, H. A., & Miller, J. S. (2011). Growth of plutons by incremental emplacement of sheets in crystal-rich host: Evidence from Miocene intrusions of the Colorado River region, Nevada, USA. *Tectonophysics*, *500*, 65–77. https://doi.org/10.1016/j.tecto.2009.07.011

Morgan, J. P., & Chen, Y. J. (1993). The genesis of oceanic crust: Magma injection, hydrothermal circulation, and crustal flow. *Journal of Geophysical Research*, *98*, 6283–6297. https://doi.org/10.1029/92jb02650

Natland, J. H., & Dick, H. J. B. (2009). Formation of the lower ocean crust and the crystallization of gabbroic cumulates at a very slowly spreading ridge. *Journal of Volcanology and Geothermal Research*, *110*, 3–4. https://doi.org/10.1016/s0377-0273(01)00211-6

Nedimović, M. R., Carbotte, S. M., Diebold, J. B., Harding, A. J., Canales, J. P., & Kent, G. M. (2008). Upper crustal evolution across the Juan de Fuca ridge flanks. *Geochemistry, Geophysics, Geosystems*, *9*(9).

Nedimović, M. R., Carbotte, S. M., Harding, A. J., Detrick, R. S., Canales, J. P., Diebold, J. B., et al. (2005). Frozen magma lenses below the oceanic crust. *Nature*, *436*(7054), 1149–1152.

Nicolas, A., Boudier, F., & France, L. (2009). Subsidence in magma chamber and the development of magmatic foliation in Oman ophiolite gabbros. *Earth and Planetary Science Letters*, *284*(1–2), 76–87. https://doi.org/10.1016/j.epsl.2009.04.012

Nicolas, A., Freydier, C., Godard, M., & Vauchez, A. (1993). Magma chambers at oceanic ridges: How large? *Geology*, *21*(1), 53–56. https://doi.org/10.1130/0091-7613(1993)021<0053:mcaorh>2.3.co;2

Nicolas, A., Reuber, I., & Benn, K. (1988). A new magma chamber model based on structural studies in the Oman ophiolite. *Tectonophysics*, *151*(1–4), 87–105. https://doi.org/10.1016/0040-1951(88)90242-9

Nooner, S. L., & Chadwick, W. W. (2016). Inflation-predictable behavior and co-eruption deformation at Axial Seamount. *Science*, *354*, 1399–1403. https://doi.org/10.1126/science.aah4666

Nooner, S. L., Webb, S. C., Buck, W. R., & Cormier, M.-H. (2014). Post eruption inflation of the East Pacific Rise at 9°50′ N. *Geochemistry, Geophysics, Geosystems*, *15*(6), 2676–2688. https://doi.org/10.1002/2014gc005389

Pallister, J. S., & Hopson, C. A. (1981). Samail ophiolite plutonic suite: Field relations, phase variation, cryptic variation and layering, and a model of a spreading ridge magma chamber. *Journal of Geophysical Research*, *86*(B4), 2593–2644. https://doi.org/10.1029/jb086ib04p02593

Rubin, K. H., & Sinton, J. M. (2007). Inferences on mid-ocean ridge thermal and magmatic structure from MORB compositions. *Earth and Planetary Science Letters*, *260*, 257–276. https://doi.org/10.1016/j.epsl.2007.05.035

Russell, J. B., Gaherty, J. B., Lin, P. Y. P., Lizarralde, D., Collins, J. A., Hirth, G., & Evans, R. L. (2019). High-resolution constraints on Pacific upper mantle petrofabric inferred from surface-wave anisotropy. *Journal of Geophysical Research: Solid Earth*, *124*(1), 631–657. https://doi.org/10.1029/2018jb016598

Shoberg, T., Stein, S., & Karsten, J. (1991). Constraints on rift propagation history at the Cobb Offset, Juan de Fuca ridge, from numerical modeling of tectonic fabric. *Tectonophysics*, *197*(2–4), 295–308. https://doi.org/10.1016/0040-1951(91)90047-V

Sinton, J. M., & Detrick, R. S. (1992). Mid-ocean ridge magma chambers. *Journal of Geophysical Research*, *97*, 197–216. https://doi.org/10.1029/91jb02508

Sparks, R. S. J., Annen, C., Blundy, J. D., Cashman, K. V., Rust, A. C., & Jackson, M. D. (2019). Formation and dynamics of magma reservoirs. *Philosophical Transactions of the Royal Society of London A*, *377*, 20180019. https://doi.org/10.1098/rsta.2018.0019

Spiegelman, M. (1993a). Flow in deformable porous media. Part 1 simple analysis. *Journal of Fluid Mechanics*, *247*, 17–38. https://doi.org/10.1017/s0022112093000369

Spiegelman, M. (1993b). Physics of melt extraction: Theory, implications and applications. *Philosophical Transactions of the Royal Society of London A*, *342*, 23–41.

Taisne, B., & Jaupart, C. (2009). Dike propagation through layered rocks. *Journal of Geophysical Research*, *114*(B9), B09203.

Toomey, D. R., Jousselin, D., Dunn, R. A., Wilcock, W. S. D., & Detrick, R. S. (2007). Skew of mantle upwelling beneath the East Pacific Rise governs segmentation. *Nature*, *446*, 409–414. https://doi.org/10.1038/nature05679

van Ark, E. M., Detrick, R. S., Canales, J. P., Carbotte, S. M., Harding, A. J., Kent, G. M., et al. (2007). Seismic structure of the Endeavour Segment, Juan de Fuca Ridge: Correlations with seismicity and hydrothermal activity. *Journal of Geophysical Research*, *112*, B02401. http://doi.org/10.1029/2005JB004210

VanTongeren, J. A., Kelemen, P. B., & Hanghøj, K. (2008). Cooling rates in the lower crust of the Oman ophiolite: Ca in olivine, revisited. *Earth and Planetary Science Letters*, *267*(1–2), 69–82. https://doi.org/10.1016/j.epsl.2007.11.034

Vera, E. E., Mutter, J. C., Buhl, P., Orcutt, J. A., Harding, A. J., Kappus, M. E., et al. (1990). The structure of 0- to 0.2-m.y.-old oceanic crust at 9ºN on the East Pacific Rise from expanded spread profiles. *Journal of Geophysical Research*, *95*, 15, 529–15, 556. https://doi.org/10.1029/jb095ib10p15529

Wanless, V. D., & Behn, M. D. (2017). Spreading rate-dependent variations in crystallization along the global mid-ocean ridge system. *Geochemistry, Geophysics, Geosystems*, *18*(8), 3016–3033. https://doi.org/10.1002/2017gc006924

Wanless, V. D., & Shaw, A. M. (2012). Lower crustal crystallization and melt evolution at mid-ocean ridges. *Nature Geoscience*, *5*(9), 651–655. https://doi.org/10.1038/ngeo1552

Wessel, P., Luis, J. F., Uieda, L., Scharroo, R., Wobbe, F., Smith, W. H. F., & Tian, D. (2019). The generic mapping tools version 6. *Geochemistry, Geophysics, Geosystems*, *20*, 5556–5564. https://doi.org/10.1029/2019gc008515

Wilcock, W. S. D., Hooft, E. E. E., Toomey, D. R., McGill, P. R., Barclay, A. H., Stakes, D. S., & Ramirez, T. M. (2009). The role of magma injection in localizing black-smoker activity. *Nature Geoscience*, *2*(7), 509–513. https://doi.org/10.1038/ngeo550

Wilcock, W. S. D., Solomon, S. C., Purdy, G. M., & Toomey, D. R. (1992). The seismic attenuation structure of a fast-spreading mid-ocean ridge. *Science*, *258*(5087), 1470–1474. https://doi.org/10.1126/science.258.5087.1470

Wilcock, W. S. D., Solomon, S. C., Purdy, G. M., & Toomey, D. R. (1995). Seismic attenuation structure of the East Pacific Rise near 9°30′N. *Journal of Geophysical Research*, *100*(B12), 24147–24165. https://doi.org/10.1029/95jb02280

Zha, Y., Webb, S. C., Nooner, S. L., & Crawford, W. C. (2014). Spatial distribution and temporal evolution of crustal melt distribution beneath the East Pacific Rise at 9°-10°N inferred from 3-D seafloor compliance modeling. *Journal of Geophysical Research: Solid Earth*, *119*(6), 4517–4537. https://doi.org/10.1002/2014jb011131